Transport and Communications Science Journal

PHASE FIELD METHOD WITH STRAIN ORTHOGONAL DECOMPOSITIONS FOR MODELLING OF DAMAGE IN HETEROGENEOUS MATERIALS OBTAINED BY X-RAY COMPUTED TOMOGRAPHY IMAGES

Vu Ba Thanh

University of Transport and Communications, No 3 Cau Giay Street, Hanoi, Vietnam

ARTICLE INFO

TYPE: Research Article
Received: 02/08/2022
Revised: 07/11/2022
Accepted: 05/12/2022
Published online: 15/01/2023
https://doi.org/10.47869/tcsj.74.1.3

* *Corresponding author*
Email: thanhvb@utc.edu.vn

Abstract. The phase-field method has become a robust tool to describe the complex crack nucleation and propagation in heterogeneous materials. In these materials, an interaction between bulk brittle damage and interfacial damage through the splitting the strain tensor into a bulk strain part and a jump strain part at the interfaces. Moreover, the material response of the heterogeneous materials in tension and compression, the bulk strain part needs to be decomposed into a positive part and a negative part. However, most of the previous works, these decompositions do not verify the negative part be orthogonal the positive part, which lead to the inaccuracy in the material mechanical behavior. To solve the shortcomings, the strain orthogonal decompositions problem that is applied to decompose the bulk strain in our work. In the present work, author combined the phase-field modeling taking into account interfacial damage with the problem of the bulk strain orthogonal decompositions by two proposed solutions. The successful prediction of the crack propagation for the inclusion-matrix structures and the multi-phases materials of X-ray computed tomography (XR-CT) images by two proposed solutions will be demonstrated in several numerical examples.

Keywords: phase field method, X-ray computed tomography, strain decompositions, interfacial damage.

1. INTRODUCTION

One of the main objectives of fracture mechanics is to predict the crack nucleation and propagation of materials. Many previous works have been done in both experimental and numerical approaches to reach this goal. Griffith [1] and Irwin [2] have placed an important milestone in the problem of predicting the crack nucleation by developing the Linear Elastic Fracture Mechanic (LEFM) theory in which the stress field is calculated using the theory of elasticity. From the stress field obtained, the stress intensity factor (SIF) is defined and the crack will grow when this stress intensity factor exceeds the material fracture toughness. Based on this theory, Francfort and Marigo [3] and Bourdin et al. [4] proposed the variational approach to fracture relative to a global minimization of the total energy allowing to numerically solve the problem determining the crack nucleation and propagation for complex structures. Then, Pham et al. [5] used the variational framework for brittle fracture with the principles of irreversibility, stability and energy balance into the phase field method to solve a homogeneous one-dimensional bar. Next, the authors of the works [6, 7] proposed a regularized description of discontinuities to replace the surface of the crack to improve the phase field modeling.

In multi-phase materials, in order to model the spread of complex cracks, especially in the interfacial zone between two phases, many previous studies have been given the Cohesive Zone Model (CZM) concept which was proposed in first by Barenblatt [8] and Dugdale [9]. Then, in the works [10], the CZM have been applied into Finite Element Method (FEM) to handle the fracture at the crack tip in brittle and ductile materials. In the CZM framework, one of the softening curves describing the relation between the traction and displacement jump across the cohesive surface as linear, exponential, hyperbolic and Cornelissen's curves can be used to determine the separation state of the cohesive surface.

In order to simulate a network of the complex cracks as well as the interface between the matrix and inclusion phases, we need to smooth the mesh size to determine accuracy the direction of the normal vectors at the nodes of elements. Several methods can find and refine the mesh size at the interfacial zone while the remaining zone can place the coarser meshes by additional functions such as viewpoint method presented in [11] and Extended Isogeometric Analysis (XIGA) in [12].

In the materials which have the highly complex microstructures and the random distribution of the multi-phases, the problem of determining the interfaces between the phases is necessary to identify the shape of the phase components. An experimental method based on the pixel-image as XR-CT is widely applied to solve this problem (see, e.g, [13, 14, 15, 16]). The phase-field modeling proposed by [17] to predict the crack propagation in realistic microstructures obtained by XR-CT gave the very reliable results. In this paper, the component phases of the realistic microstructure obtained by XR-CT are recognized by a supplemental sub-function [18] from the *.jpg image formats.

A recent theoretical study of He and Shao [19] proposed the strain decomposition into a negative and positive parts which are orthogonal in the sense of an inner product where the elastic stiffness tensor acts as a metric tensor. These strain orthogonal decompositions described accuracy in mechanical behaviors of materials. In this work, we used the strain decomposition proposed in [19] associated with the work [17] to improve accuracy in terms of mechanical behaviors in the multi-phase materials. The principal advantages of this method are: (a) the orthogonality condition is applied to the bulk strain decomposition; (b) multiple complex crack

nucleation and propagation of the realistic materials obtained by XR-CT can be solved in the interaction between the bulk crack and interfacial one; (c) two solutions based on orthogonality condition are applied for the phase field method (denoted by Solution 1 and Solution 2).

The overview of the paper is as follows: Section 2 gives the detailed phase-field framework taking into account the interfacial damage associated with the strain orthogonal decompositions. In Section 3, several numerical examples using two solutions are presented. Finally, conclusions and perspectives are drawn in Section 4.

2. PHASE FIELD METHOD OF BULK DAMAGE AND INTERFACIAL DAMAGE WITH THE STRAIN ORTHOGONAL DECOMPOSITIONS

2.1. Regularized form of the energy in the phase field method

In this simulation method, the general form of the energy in the cracked structure is described by:

$$\Pi(\mathbf{u},\phi,\alpha)=\int_{\Omega}\bar{\Psi}(\mathbf{u},\phi,\alpha)d\Omega \tag{1}$$

in which:

$$\bar{\Psi}(\mathbf{u},\phi,\alpha)=\bar{\Psi}_u^e(\mathbf{E}_e,\phi)+\{1-\alpha\}G_c\gamma(\phi,\nabla\phi)+\bar{\Psi}^{\text{int}}\left(\ \mathbf{u}\ ,\alpha\right)\gamma_\alpha(\alpha,\nabla\alpha) \tag{2}$$

where, the strain tensor $\mathbf{E}=\nabla^s(\mathbf{u})_{ij}=\frac{1}{2}\left(u_{i,j}+u_{j,i}\right)$ is decomposed into two parts related to the bulk $\mathbf{E}_e$ and the displacement jump at the interface $\bar{\mathbf{E}}$, respectively:

$$\mathbf{E}(\mathbf{u}(\mathbf{x}))=\mathbf{E}_e(\mathbf{u}(\mathbf{x}))+\bar{\mathbf{E}}(\ \mathbf{u}\ (\mathbf{x})) \tag{3}$$

And $\bar{\Psi}_u^e(\mathbf{E}_e,\phi)$ is the strain density function, which relates to the tension and compression elastic strain energy parts $\bar{\Psi}_e^+$ and $\bar{\Psi}_e^-$:

$$\bar{\Psi}_u^e(\mathbf{E}_e,\phi)=\bar{\Psi}_e^+(\mathbf{E}_e^+)\{g(\phi)+\kappa\}+\bar{\Psi}_e^-(\mathbf{E}_e^-) \tag{4}$$

We used the widely degradation function $g(\phi)=(1-\phi)^2$, with $\kappa \ll 1$ is a small parameter to ensure the well-posedness of the system in a broken solid. Here, the phase field variables $\phi(\mathbf{x})$ and $\alpha(\mathbf{x})$) describing the damage of the solid and the interface, respectively:

$$\phi(\mathbf{x},t)=Arg\left\{\inf_{\phi\in\mathcal{S}_\phi}\left(\Gamma_\phi(\phi)\right)\right\},\ \mathcal{S}_\phi=\left\{\phi\,|\,\phi(\mathbf{x})=1\ \text{ on }\ \Gamma,\forall\mathbf{x}\in\Gamma\right\} \tag{5}$$

$$\alpha(\mathbf{x},t)=Arg\left\{\inf_{\alpha\in\mathcal{S}_\alpha}\left(\Gamma_\alpha(\alpha)\right)\right\},\ \mathcal{S}_\alpha=\left\{\alpha\,|\,\alpha(\mathbf{x})=1\ \text{ on }\ \Gamma^{\text{int}},\forall\mathbf{x}\in\Gamma^{\text{int}}\right\} \tag{6}$$

In the equations (5) and (6), Γ^{int} and Γ be an interface between the different phases and the crack surfaces, respectively**,** $\mathbf{u}(\mathbf{x})$ is the displacement variable, $\bar{\Psi}^{\text{int}}$ is a strain density function depending on the displacement jump across the interface; $\mathbf{u}$ is the displacement jump at the

interface; G_c is the fracture resistance. The same regularization length $\eta = \eta_\alpha = \eta_\phi$ is adopted for the interfacial crack and the bulk crack for the sake of simplicity, thus $\gamma(\phi, \nabla\phi) = \frac{\phi^2}{2\eta} + \frac{\eta}{2}\nabla\phi \cdot \nabla\phi$ and $\gamma_\alpha(\alpha, \nabla\alpha) = \frac{\alpha^2}{2\eta} + \frac{\eta}{2}\nabla\alpha \cdot \nabla\alpha$ are the crack surface density functions which depend on $\phi(\mathbf{x})$ and $\alpha(\mathbf{x})$.

In this work, the bulk strain $\mathbf{E}_e$ is decomposed into the tension part $\mathbf{E}_e^+$ and the compression part $\mathbf{E}_e^-$ as follows:

$$\mathbf{E}_e = \mathbf{E}_e^+ + \mathbf{E}_e^- \tag{7}$$

Base on the principle of maximum dissipation and energy minimization of [3] and the boundary conditions of the variables $\phi(\mathbf{x})$, $\alpha(\mathbf{x})$ and $\mathbf{u}(\mathbf{x})$ in [17], we solve two systems of equations to determine the variables $\phi(\mathbf{x})$ and $\mathbf{u}(\mathbf{x})$, respectively:

$$\begin{cases} 2(1-\phi)\mathcal{H}^e - (1-\alpha)\dfrac{G_c}{\eta}(\phi - \eta^2\Delta\phi) = 0 \ \text{ in } \Omega \\ \phi(\mathbf{x}) = 1 \qquad\qquad\qquad\qquad \text{on } \Gamma \\ \nabla\phi(\mathbf{x}).\mathbf{n} = 0 \qquad\qquad\qquad\qquad \text{on } \partial\Omega \end{cases} \tag{8}$$

and

$$\begin{cases} \nabla.\boldsymbol{\sigma}_e(\mathbf{u}, \phi) + h\gamma_\alpha \nabla\mathbf{t}(\ \mathbf{u}\ )\mathbf{n}^I = \mathbf{f} \ \text{ in } \Omega \\ \mathbf{u} = \bar{\mathbf{u}} \qquad\qquad\qquad\qquad \text{on } \partial\Omega_u \\ \boldsymbol{\sigma}_e.\mathbf{n} = \bar{\mathbf{F}} \qquad\qquad\qquad\qquad \text{on } \partial\Omega_F \end{cases} \tag{9}$$

In (9), $\boldsymbol{\sigma}_e = \dfrac{\partial\bar{\Psi}_u^e(\mathbf{E}_e, \phi)}{\partial\mathbf{E}_e}$ is the Cauchy stress tensor, $\mathbf{f}$ are body forces and $\bar{\mathbf{u}}$ and $\bar{\mathbf{F}}$ are prescribed displacements and forces on the corresponding boundaries $\partial\Omega_u$ and $\partial\Omega_F$, respectively. And $\mathbf{t}(\ \mathbf{u}\ ) = \dfrac{\partial\bar{\Psi}^{\text{int}}(\ \mathbf{u}\ )}{\partial\ \mathbf{u}}$ is the traction stress at the interface. Then, we set $\mathbf{t}(\ \mathbf{u}\ ) = \left[t_n, t_t\right]^T$ with t_n and t_t are the normal and tangential parts (see [17]). In (9), (10), $\nabla.(\bullet), \nabla(\bullet)$ and $\Delta(\bullet)$ are gradient, divergence and laplace of $(\bullet)$; $\mathbf{n}^I$ and $\mathbf{n}$ are the normal vectors to Γ^{int} and the external boundary of the domain Ω, respectively.

The equation (8^1) associated weak form is determined as:

$$\int_\Omega \left\{ \left(2\mathcal{H}^e + (1-\alpha)\frac{G_c}{\eta} \right)\phi\delta\phi + (1-\alpha)G_c\eta\nabla\phi.\nabla(\delta\phi) \right\} d\Omega = \int_\Omega 2\mathcal{H}^e\delta\phi d\Omega \tag{10}$$

where, the strain history function $\mathcal{H}^e$ is defined as:

$$\mathcal{H}^e = \max_{\tau\in[0,t]}\left\{\bar{\Psi}_e^+\left(\mathbf{x},\tau\right)\right\} \tag{11}$$

2.2. Strain orthogonal decompositions implemented into phase field method

The strain orthogonal decomposition is presented in [19] which is applied to the bulk strain $\mathbf{E}_e$. This orthogonal condition is implemented within the phase field method with interfacial damage [17]. Let $\mathbb{C}$ be the fourth-order stiffness tensor, two elastic strain energy parts $\bar{\Psi}_e^+$ and $\bar{\Psi}_e^-$ are expressed by:

$$\bar{\Psi}_e^{\pm}(\mathbf{E}_e) = \frac{1}{2}\mathbf{E}_e^{\pm} : \left(\mathbb{C} : \mathbf{E}_e^{\pm}\right) = \frac{1}{2}\,\tilde{\mathbf{E}}_e^{\pm} : \tilde{\mathbf{E}}_e^{\pm} \tag{12}$$

where, $\tilde{\mathbf{E}}_e^{\pm} = \mathbb{C}^{1/2} : \mathbf{E}_e^{\pm}$ and the tension and compression parts $\mathbf{E}_e^+$ and $\mathbf{E}_e^-$ must be satisfied the following conditions:

$$\tilde{\mathbf{E}}_e = \tilde{\mathbf{E}}_e^+ + \tilde{\mathbf{E}}_e^- \text{ and } \tilde{\mathbf{E}}_e^+ : \tilde{\mathbf{E}}_e^- = 0 \tag{13}$$

We have solution 1 and solution 2 which satisfy the orthogonality condition (13) as follows:

Solution 1: two parts $\tilde{\mathbf{E}}_e^{\pm}$ are analyzed as:

$$\tilde{\mathbf{E}}_e^+ = \frac{1}{\mathcal{D}}\left\langle \mathrm{Tr}\left(\tilde{\mathbf{E}}_e\right)\right\rangle_+ \mathbf{1} + \tilde{\mathbf{E}}_e^{dev}; \text{ and } \tilde{\mathbf{E}}_e^- = \frac{1}{\mathcal{D}}\left\langle \mathrm{Tr}\left(\tilde{\mathbf{E}}_e\right)\right\rangle_- \mathbf{1} \tag{14}$$

Where, $\mathbf{1}$ denotes the $\mathcal{D}$- dimensional identity tensor ($\mathcal{D}=2,3$ in the cases 2D and 3D, respectively), $\langle x\rangle_{\pm} = \left(x \pm |x|\right)/2$ and the deviatoric strain tensor is $\tilde{\mathbf{E}}_e^{dev} = \tilde{\mathbf{E}}_e - \frac{1}{\mathcal{D}}\mathrm{Tr}\left(\tilde{\mathbf{E}}_e\right)\mathbf{1}$.

The positive and negative strain energy density functions $\bar{\Psi}_e^+$ and can be obtained:

$$\bar{\Psi}_e^+(\mathbf{E}_e^+) = \frac{1}{2}\,\tilde{\mathbf{E}}_e^+ : \tilde{\mathbf{E}}_e^+ = \frac{1}{2}\left\{\frac{1}{\mathcal{D}}\left\langle \mathrm{Tr}\left(\tilde{\mathbf{E}}_e\right)\right\rangle_+ \mathbf{1} + \tilde{\mathbf{E}}_e^{dev}\right\} : \left\{\frac{1}{\mathcal{D}}\left\langle \mathrm{Tr}\left(\tilde{\mathbf{E}}_e\right)\right\rangle_+ \mathbf{1} + \tilde{\mathbf{E}}_e^{dev}\right\} \tag{15}$$

and

$$\bar{\Psi}_e^-(\mathbf{E}_e^-) = \frac{1}{2}\,\tilde{\mathbf{E}}_e^- : \tilde{\mathbf{E}}_e^- = \frac{1}{2}\left\{\frac{1}{\mathcal{D}}\left\langle \mathrm{Tr}\left(\tilde{\mathbf{E}}_e\right)\right\rangle_- \mathbf{1}\right\} : \left\{\frac{1}{\mathcal{D}}\left\langle \mathrm{Tr}\left(\tilde{\mathbf{E}}_e\right)\right\rangle_- \mathbf{1}\right\} \tag{16}$$

The Cauchy stress is defined as:

$$\boldsymbol{\sigma}_e = \frac{\partial \bar{\Psi}_e^+(\mathbf{E}_e^+)}{\partial \mathbf{E}_e}\left(g(\phi)+\kappa\right) + \frac{\partial \bar{\Psi}_e^-(\mathbf{E}_e^-)}{\partial \mathbf{E}_e} = \left\{\left(g(\phi)+\kappa\right)\mathbf{r}_e^+ : \mathbb{C} : \mathbf{r}_e^+ + \mathbf{r}_e^- : \mathbb{C} : \mathbf{r}_e^-\right\} : \mathbf{E}_e \tag{17}$$

In the equations (15), (16) and (17), $\mathbf{r}_e^+ = \left\{\frac{\tilde{\mathbf{r}}_e^+}{\mathcal{D}}[\mathbf{1}]^T[\mathbf{1}] + \left(\mathbf{I} - \frac{[\mathbf{1}]^T[\mathbf{1}]}{\mathcal{D}}\right)\right\}$, $\mathbf{r}_e^- = \left\{\frac{\tilde{\mathbf{r}}_e^-}{\mathcal{D}}[\mathbf{1}]^T[\mathbf{1}]\right\}$ and

$\left\langle \mathrm{Tr}\left(\tilde{\mathbf{E}}_e\right)\right\rangle_{\pm} = \tilde{\mathbf{r}}_e^{\pm}\mathrm{Tr}\left(\tilde{\mathbf{E}}_e\right)$ with $\tilde{\mathbf{r}}_e^{\pm} = \frac{1}{2}\left\{\mathrm{sign}\left\{\pm\mathrm{Tr}\left(\tilde{\mathbf{E}}_e\right)\right\}+1\right\}$.

Solution 2: two parts $\tilde{\mathbf{E}}_e^{\pm}$ are defined as:

$$\tilde{\mathbf{E}}_e^{\pm} = \sum_{i=1}^{\mathcal{D}}\left\langle \tilde{E}_e^i\right\rangle_{\pm}\tilde{\mathbf{n}}_i\otimes\tilde{\mathbf{n}}_i \tag{18}$$

Where, $\tilde{E}_e^i$ and $\tilde{\mathbf{n}}_i$ with $i=1,...,\mathcal{D}$ are the ordered eigenvalues and eigenvectors of $\tilde{\mathbf{E}}_e^{\pm}$.

Two parts of the strain energy density function in the second case are concerned:

$$\bar{\Psi}_e^{\pm}(\mathbf{E}_e^{\pm}) = \frac{1}{2}\left(\mathbb{C}^{1/2}\,\mathbf{E}_e^{\pm}\right):\left(\mathbb{C}^{1/2}\,\mathbf{E}_e^{\pm}\right) = \frac{1}{2}\tilde{\mathbf{E}}_e^{\pm}:\tilde{\mathbf{E}}_e^{\pm} \tag{19}$$

In this solution, the Cauchy stress is written as:

$$\begin{aligned}\boldsymbol{\sigma}_e &= \frac{\partial\bar{\Psi}_e^{+}(\mathbf{E}_e^{+})}{\partial\mathbf{E}_e}\left(g(\phi)+\kappa\right)+\frac{\partial\bar{\Psi}_e^{-}(\mathbf{E}_e^{-})}{\partial\mathbf{E}_e} \\ &= \left\{\left(g(\phi)+\kappa\right)\left(\tilde{\mathbb{Q}}_e^{+}:\mathbb{C}^{1/2}\right):\left(\tilde{\mathbb{Q}}_e^{+}:\mathbb{C}^{1/2}\right)+\left(\tilde{\mathbb{Q}}_e^{-}:\mathbb{C}^{1/2}\right):\left(\tilde{\mathbb{Q}}_e^{-}:\mathbb{C}^{1/2}\right)\right\}:\mathbf{E}_e\end{aligned} \tag{20}$$

From equation (20), $\tilde{\mathbb{Q}}_e^{\pm}$ are two projectors defined as $\tilde{\mathbb{Q}}_e^{\pm} = \frac{\partial\tilde{\mathbf{E}}_e^{\pm}}{\partial\tilde{\mathbf{E}}_e}$.

We solve the systems of equations (8) and (9) by a finite element method in a staggered scheme with the load increments [17].

3. NUMERICAL EXAMPLES

3.1. Symmetric three-point bending test

This example aims to study the crack propagation within a beam during a three-point bending test. Furthermore, two solutions of strain decompositions (14) and (18) are investigated in this study. The beam under consideration in this study is assumed to have the same dimensions as the one used in [17] and [20]. The geometry of the structure and the loading conditions are depicted in Fig.1. The domain has an initial cohesive interface to validate the cohesive model. The dimensions of the beam are 10x3mm. The domain occupied by the beam is uniformly meshed into 200x60 quadrilateral elements. The boundary conditions are as follows: the left bottom corner is fixed in two directions, while the right bottom corner the vertical displacement is fixed, and the horizontal displacement is free. The displacement is prescribed at the center on the upper end of the beam with monotonic increments of the displacement Δu = -0.005 mm for 170 load increments.

The material properties of the beam are chosen as $E = 100\text{MPa}$, $\upsilon = 0.3$, the fracture toughness in the phases and the interface $G_c = G_c^I = 0.1\text{N/mm}$, the fracture strength at the interface Γ^{int} is set as $t_u = 1\text{MPa}$ (see [17]). The regularization parameter η is chosen as η = 0.15mm. The plane strain assumption is adopted in our simulation.

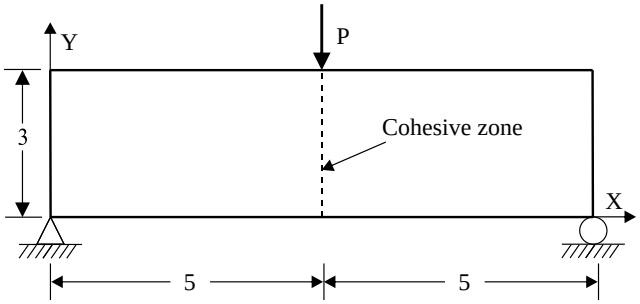

Figure 1. Symmetric three-point bending test: geometry and boundary conditions.

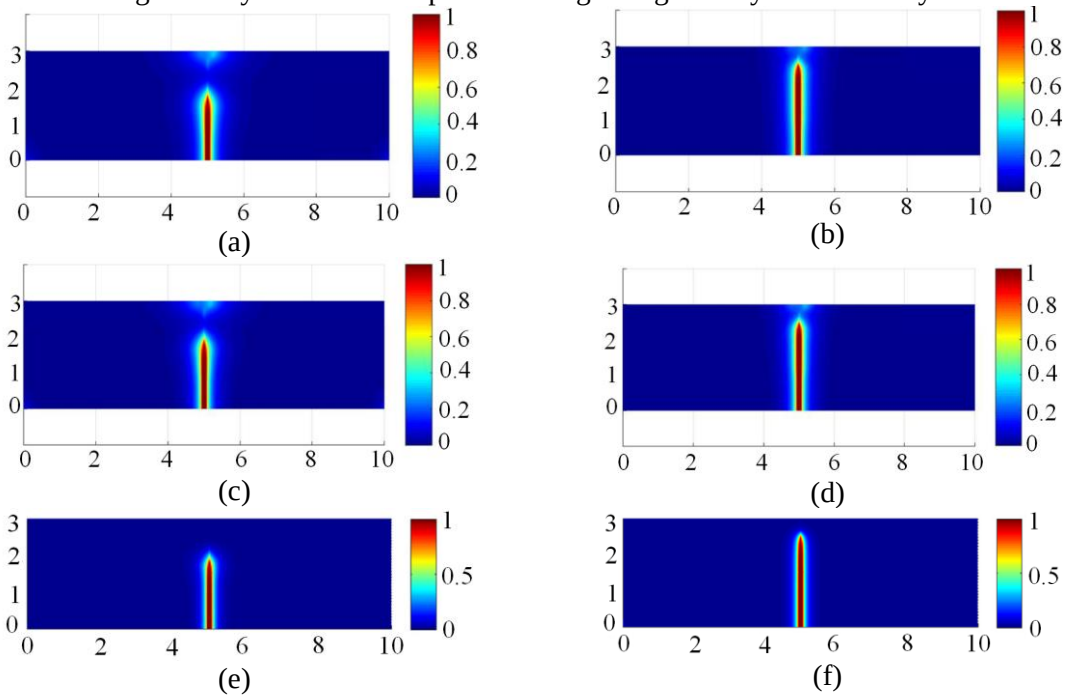

Figure 2. The crack evolution in the symmetric three-point bending test: solution 1 (a) 0.25 mm, (b) 0.35 mm; solution 2 (c) 0.25 mm, (d) 0.35 mm; Nguyen et al. [17] (e) 0.25 mm, (f) 0.35 mm.

By applying two solutions of strain decompositions (14) and (18), the evolutions of the crack are shown in Fig. 2(a-b) and Fig. 2(c-d) with different values of the prescribed displacement at the center on the upper end of the beam. These crack evolutions obtained in the work [17] are also presented in Fig. 2(e-f). The comparison of the load-displacement curves between two solutions of strain decompositions (14) and (18) with the results derived in [17, 20] is shown in Fig. 3. From the comparison of both the evolution of the crack and the mechanical behavior in Fig. 2 and Fig. 3, we can see that the present method with two proposed strain decompositions (14) and (18) are practically efficient and accurate to simulate the crack propagation with the influence the interfacial damage.

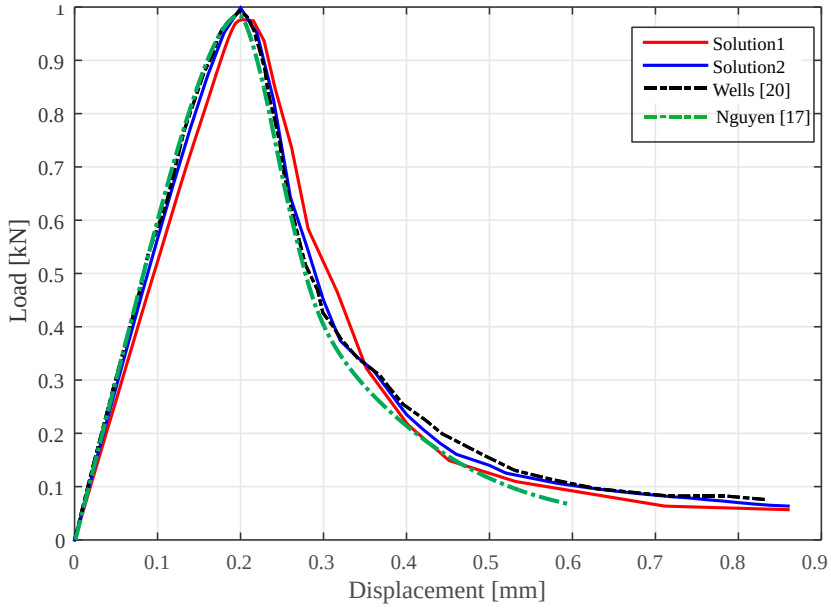

Figure 3. Symmetric three-point bending test: comparison of the load-displacement curves between [17], [20] with two solutions of strain orthogonal decompositions (14) and (18).

3.2. Tension test of a plate containing randomly distributed inclusions

This example aims to simulate the development of the interfacial damage situated between the randomly distributed inclusions and matrix phases. For this purpose, we use a plate containing 9 randomly distributed circular inclusions whose volume fraction is equal to 0.07. The dimensions of the plate are 1x1mm. On the lower end, the vertical displacements are fixed, while the horizontal displacements are free and the left bottom node is fixed. On the upper end, the vertical displacements are prescribed in such a way that their values increase monotonically with $\Delta u = 0.00005\,\text{mm}$ during 200 load increments (see Fig. 4). The material properties of the inclusion and matrix phases are chosen, respectively: $E_i = 52\,\text{GPa}$, $\upsilon_i = 0.3$, $E_m = 10.4\,\text{GPa}$, $\upsilon_i = 0.3$, $t_u = 0.01\,\text{GPa}$. The toughnesses of both phases and the interface are taken as $G_c = G_c^I = 0.27\ \text{N/mm}$. The plane strain assumption is considered.

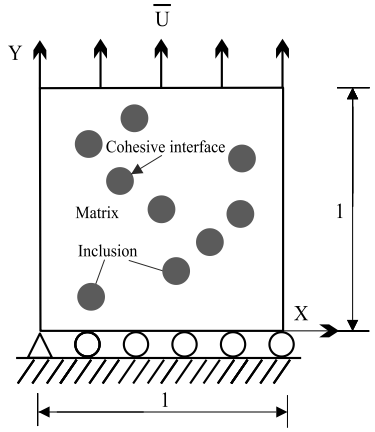

Figure 4. Traction test of a microstructure containing randomly distributed inclusions: geometry and boundary conditions.

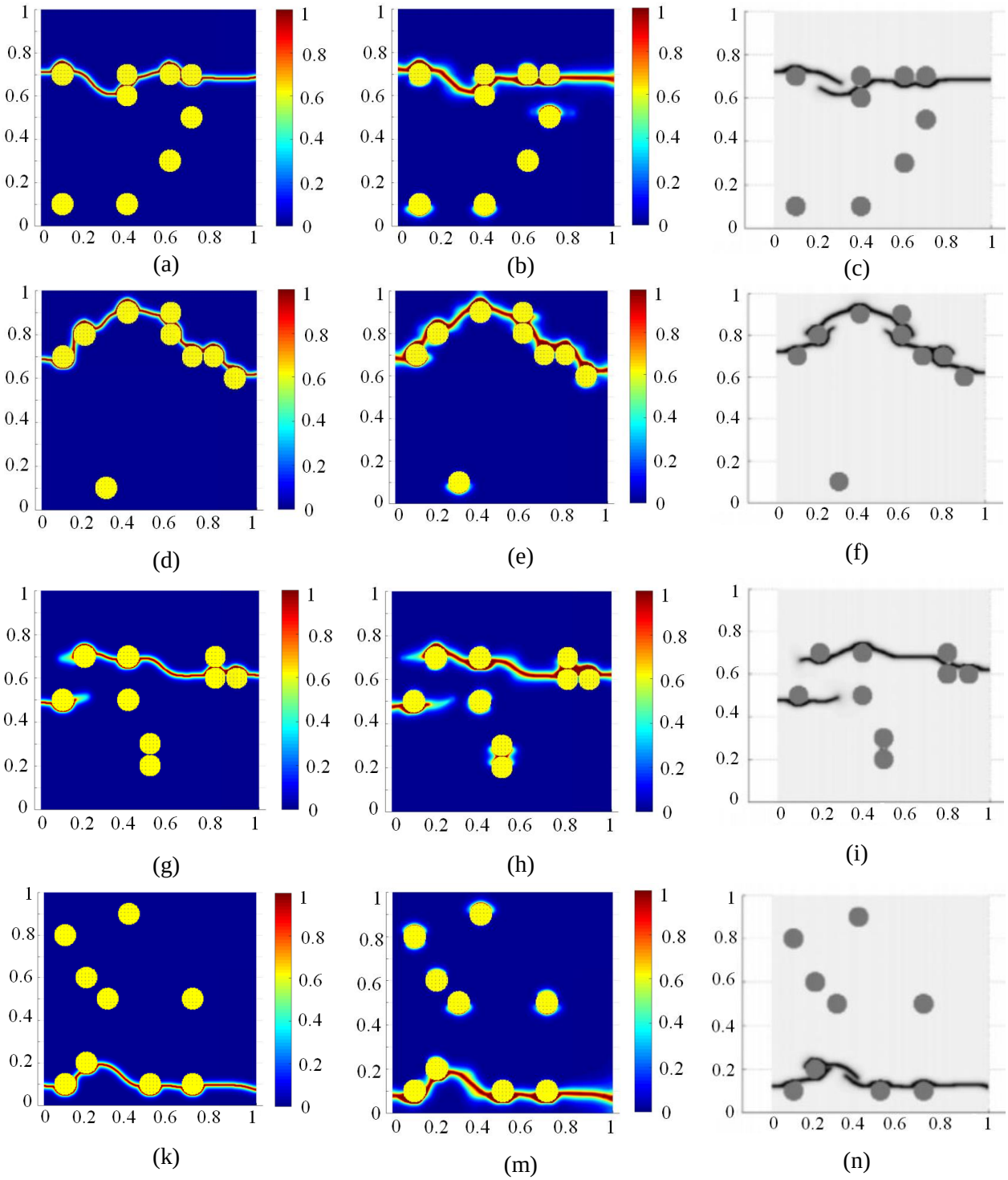

Figure 5. Crack evolution for several representation realizations of the microstructures containing randomly distributed inclusions: (a), (d), (g) and (k) Solution 1; (b), (e), (h) and (m) Solution 2; (c), (f), (i) and (n) Nguyen et al. [17].

The structure is discretized into 300x300 quadrilateral elements. The regularization parameter is chosen as $\eta = 0.0075\,\text{mm}$. In this example, we simulate the crack evolution of 15 realizations of this plate containing 9 randomly distributed inclusions. The microcracking

propagations of several representation realizations are shown in Fig. 5. It can be seen that, the evolutions of the crack are very various: when the inclusions in contact with each other, the crack path is intiated between the inclusions where mechanical behavior seems to be the weakest, in the contrast when the inclusions are not in contact, the crack path can be created at the interface between the matrix and the inclusions, and then propagate into the matrix until the fully damage. We can see that when using the two proposed solutions, the main cracks are the continuous lines without dividing into two crack ends as [17]. This phenomenon is completely natural in brittle materials in tension. This can be explained that with two present solutions, they are possible to eliminate the singularity points on the behavior curve and the spurious effect in the structure when is close to complete damage. This will improve the precision in the mechanical behavior of these materials.

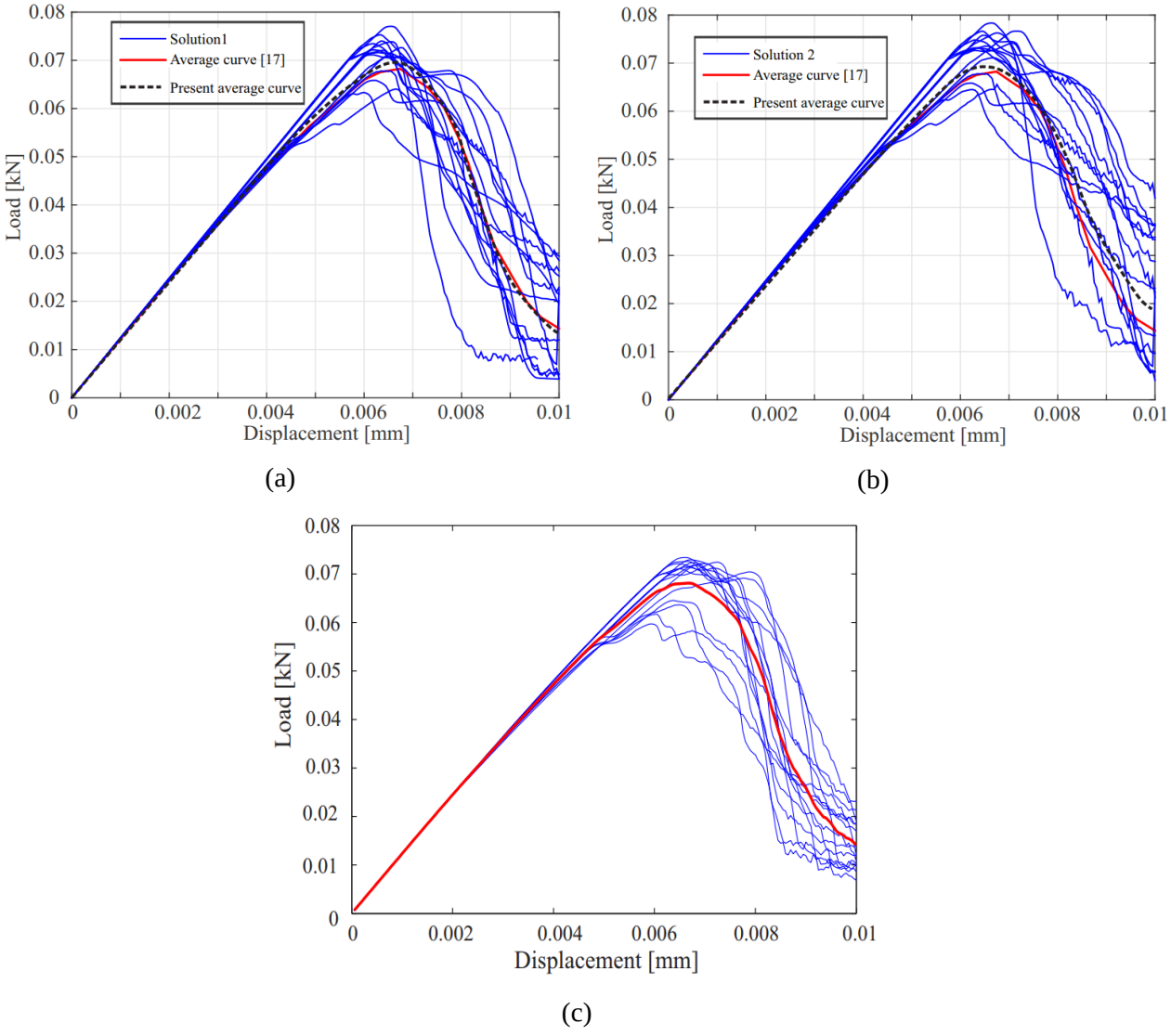

Figure 6. Comparison of the load-displacement curves (the red curve and dash line denote the average response [17] and the present average response, respectively): (a) behavior curves for 15 realizations with solution 1; (b) behavior curves for 15 realizations with solution 2; (c) behavior curves for 15 realizations with Nguyen et al. [17].

The load-displacement curves of two proposed solutions and [17] are plotted in Fig. 6a-c for 15 realizations. The average responses of [17] and the present solutions for 15 realizations are shown in the red line and the dash line, respectively. From the obtained results of both the crack propagation and the mechanical behaviors in the simulation for 15 realizations, two present solutions of strain orthogonal decompositions can provide a promising tool to investigate the damage of more complex structures.

3.3. Tension test of a realistic microstructure obtained by XR-CT images

In this example, we use two proposed strain decompositions (14) and (18), to predict the microcrack propagation with both interfacial damage and bulk damage of a realistic microstructure obtained by XR-CT image. We consider a 2D microstructure of dimensions 37.2x37.2mm. By using the XR-CT image of a real cementitious material provided in [16], the geometry of this structure is described in Fig. 7a. The realistic material consists three phases: mortar (grey), gravel aggregates (black) and pore (white). The loading conditions in the horizontal and vertical directions are illustrated in Fig. 7b and Fig. 7c, respectively. The *.jpg file of Fig. 7a is recognized by a supplemental sub-function [18], we have the shapes of three phases after the processing: mortar (blue), gravel aggregates (black) and pore (white) which are presented in Fig. 8a. Then, a numerical technique of a level-set function [17] is used to determine the complex interface of the aggregates and mortar (see Fig. 8b). The objective of the interface determination is to handle the value of varible $\alpha(\mathbf{x})$ from Eq. (6). After the process of the mesh discretization, the corresponding volume fractions of pores, aggregates and cement paste are 0.48%, 51.27% and 48,25%, which satisfy the volume fractions from 0.47% to 0.50% for pores, from 50.72% to 51.84% for aggregates, and 48.81% to 47.66% for cement paste in [16].

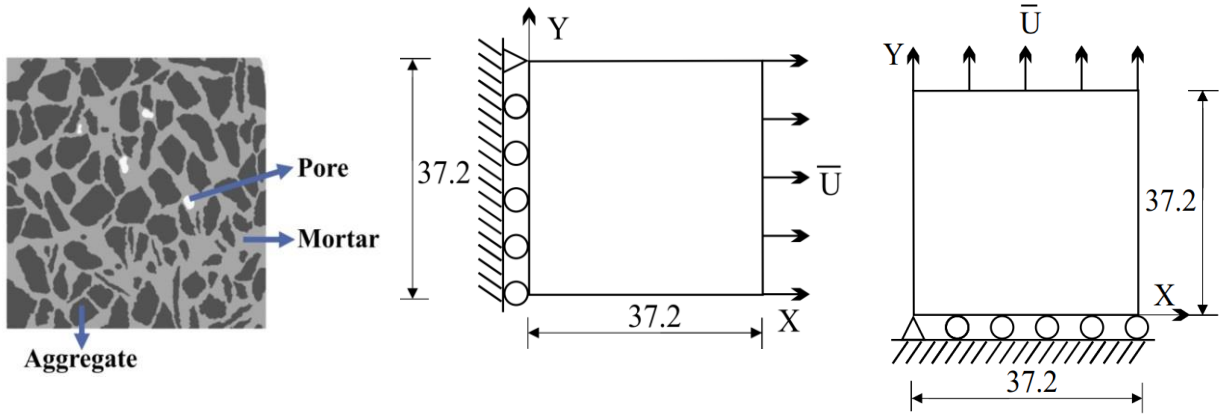

(a) (b) (c)

Figure 7. Tension test of a realistic microstructure obtained by XR-CT: geometry and loading conditions: (a) XR-CT image in Ren et al. [16]; (b) horizontal tension test; (c) vertical tension test.

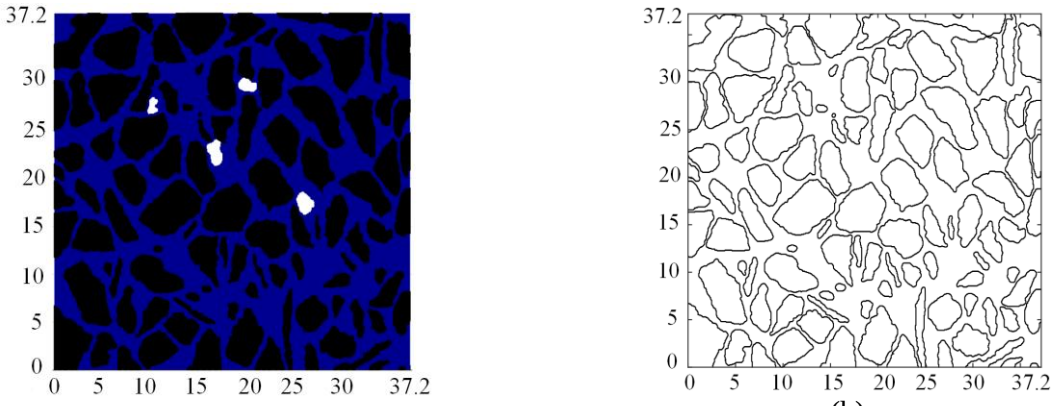

Figure 8. A microstructure obtained by XR-CT: (a) the shapes of three phases is recognized by [18]: mortar (blue), aggregates (black) and pores (white); (b) zero isovalue is solved by a level-set [17].

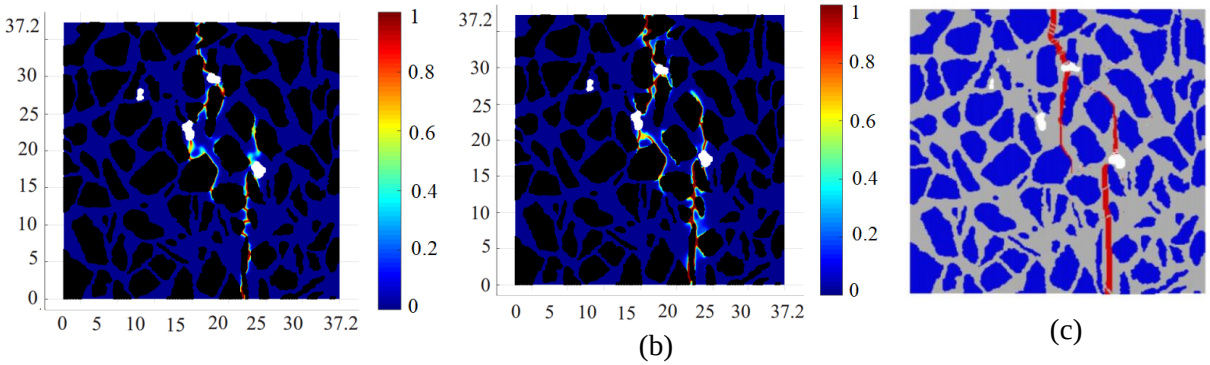

Figure 9. Horizotal tension test: the crack initiation and propagation: (a) solution 1; (b) solution 2; (c) Ren et al. [16].

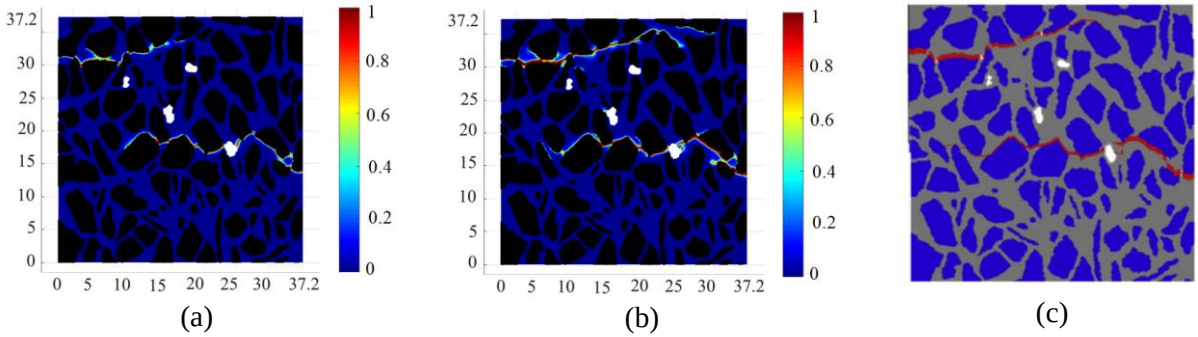

Figure 10. Vertical tension test: the crack initiation and propagation: (a) solution 1; (b) solution 2; (c) Ren et al. [16].

The material parameters of aggregate and mortar are $E_i = 70\,\text{GPa}$, $\upsilon_i = 0.2$, $E_m = 25\,\text{GPa}$ and $\upsilon_m = 0.2$. The toughness $G_c = G_c^I = 30\ \text{N/m}$. The fracture strength is taken as $t_u = 3\,\text{MPa}$ (see in [16]). We can choose the very compliant properties for the pore as $E_p = 10^{-6}\ \text{GPa}$, $\upsilon_p = 0.2$. In the horizontal and vertical tension tests, we use the constant displacement increments $\Delta u = 2x10^{-6}\ \text{mm}$ during 240 load increments. The structure is discretized into 600x600 quadrilateral elements. The regularization parameter is chosen as $\eta = 0.13\,\text{mm}$. The evolutions of

crack for the horizontal tension test with two solutions of strain decompositions (14) and (18) and the ones obtained in [16] are shown in Fig. 9a-c, respectively. The crack evolutions for the vertical tension test are presented in Fig. 10. Meanwhile, Fig. 11 shows the comparison of the stress- strain curves of the horizontal tension test and the vertical tension test between [16] with two proposed solutions. In Fig. 11, the stress is calculated by dividing the total nodal reaction load of all the nodes on the boundary by the side length of the microstructure, and the strain is the ratio of the resultant displacement prescribed at the side of the microstructure to its side length.

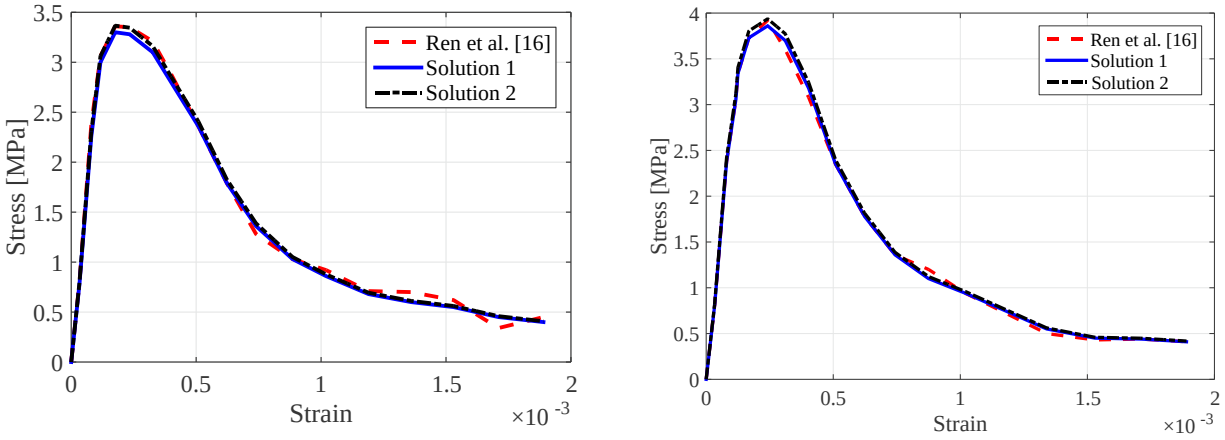

Figure 11. Comparison of the load-displacement curves between [16] with two solutions of strain orthogonal decompositions (14) and (18): (a) horizontal tension test; (b) vertical tension test.

From two proposed strain decompositions (14) and (18), several cracks nucleate at the pores, while other cracks initiate at the interface of the phases and then spread into the matrix until the fully damage during the displacement increments (see Figs. 9-10). The obtained results are very similar to the experimental results presented in [16]. Furthermore, in Fig. 11, it can be seen that the stress-strain relationships with two solutions of strain decompositions (14) and (18) exhibit a good agreement with ones provided in [16]. Moreover, the behavior curves of two present solutions are smoother than that of [16], especially, when the microstructure is nearly fully damage. This can be explained that, two strain orthogonal decompositions of this paper can eliminate the singularity points on the behavior curve and the spurious effect in the microstructure in the damage process to improve the accuracy of material behaviors.

The obtained results of the crack paths and the behavior curves demonstrate the present numerical modelling are the robust tools to predict the complex crack paths in the interaction of the bulk damage and the interfacial damage in the realistic microstructure obtained by XR-CT.

4. CONCLUSION AND PERSPECTIVES

In this work, we have applied two strain orthogonal decompositions into the phase-field with the interfacial damage to simulate the fracture in the very complex and heterogeneous material. The first example in which the interface between two structural domains is assumed to be simple and smooth, the crack nucleation and propagation are very efficient and accurate.

In the second example of the microstructure containing randomly distributed inclusions with their various shapes of the interface and randomly occurrence densities, the microcrack is created

not only by interfacial damage and but also by the bulk damage. The simulation of the crack with two proposed solutions of strain orthogonal decompositions is a good tool to predict the crack propagation in composites with complex microstructures.

In the last example, we have simulated the damage in a realistic microstructure obtained by XR-CT. This microstructure contains multi-phases: mortar, aggregates, and pore. The numerical techniques like a level-set function and a supplemental sub-function are used to determine the arbitrary shape of the interfaces. In this paper, the strain orthogonal decompositions of [19] have used and implemented in this phase field modelling with two proposed solutions. This helps to eliminate the singularity points on the behavior curve and the spurious effect in the structure in the damage process to improve the accuracy of material responses.

However, all the numerical examples given in this paper are two-dimensional, and the materials considered are brittle or quasi-brittle. In principle, the methods developed in this paper are valid in the three-dimensional situation but this should be carried out in a near future. The extension of our work beyond brittle or quasi-brittle materials necessitates more effort. For example, considering viscoelasticity and plasticity is challenging, especially in the anisotropic case.

ACKNOWLEDGMENT

This research is funded by University of Transport and Communications (UTC) under grant number T2022-CT-005TD.

REFERENCES

[1]. G.A. Griffith, The phenomena of rupture and flow in solid, Philosophical Transaction of the Royal Society London Series A, 221 (1921) 163-198. https://doi.org/10.1098/rsta.1921.0006

[2]. G.R. Irwin, Analysis of stress and strains near the end of a crack traversing a plate, J. Appl. Mech, 24 (1957) 361-364.

[3]. G.A. Francfort, J.J. Marigo, Revisiting brittle fracture as an energy minimization problem, J. Mech. Phys. Solids, 46 (1998), 1319-1342. https://doi.org/10.1016/S0022-5096(98)00034-9

[4]. B. Bourdin, J.J. Marigo, C. Maurini, P. Sicsic, Morphogenesis and propagation of complex cracks induced by thermal shocks, Phys. Rev. Lett, 112 (2014) 014301. https://doi.org/10.1103/PhysRevLett.112.014301

[5]. K. Pham, J.J. Marigo, C. Maurini, The issues of the uniqueness and the stability of the homogeneous response in uniaxial tests with gradient damage models, J. Mech. Phys. Solids, 59 (2011b) 1163-1190. https://doi.org/10.1016/j.jmps.2011.03.010

[6]. D. Mumford, J. Shah, Optimal approximations by piecewise smooth functions and associated variational problems, Commun. Pure. Appl. Math, 42 (1989) 577-685. https://doi.org/10.1002/cpa.3160420503

[7]. C. Miehe, M. Hofacker, F. Welschinger, A phase field model for rate-independent crack propagation: robust algorithmic implementation based on operator splits, Comput. Methods Appl. Mech. Eng, 199 (2010) 2765-2778. https://doi.org/10.1016/j.cma.2010.04.011

[8]. G.I. Barenblatt, The formation of equilibrium cracks during brittle fracture. General ideas and hypotheses. Axially-symmetric cracks, J. Appl. Math. Mech, 23 (1959) 622–636.

[8]. D.S. Dugdale, Yielding of steel sheets containing slits, J. Mech. Phys. Solids, 8 (1960) 100–104. https://doi.org/10.1016/0022-5096(60)90013-2

[10]. C.V. Verhoosel, R. de Borst, A phase-field model for cohesive fracture, Internat. J. Numer. Methods Engrg, 96 (2013) 43–62. https://doi.org/10.1002/nme.4553

[11]. N. Sukumar, N. Moes, B. Moran, T. Belytschko, Extended finite element method for threedimensional crack modelling, Internat. J. Numer. Methods Engg, 48 (2000) 1549-1570. https://doi.org/10.1002/1097-0207(20000820)48:11<1549::AID-NME955>3.0.CO;2-A

[12]. J. Gu, T. Yu, V.L. Le, T.T. Nguyen, S. Tanaka, Q.T. Bui, Multi-inclusions modeling by adaptive XIGA based on LR B-splines and multiple level sets, Finite Elem. Anal. Des, 148 (2018) 48-66. https://doi.org/10.1016/j.finel.2018.05.003

[13]. W.D. Carlson,Three-dimensional imaging of earth and planetary materials, Earth Planet Sci. Lett, 249 (2006) 133-147. https://doi.org/10.1016/j.epsl.2006.06.020

[14]. L. Babout, T.J. Marrow, D. Engelberg, P.J. Withers, X-ray microtomographic observation of intergranular stress corrosion cracking in sensitised austenitic stainless steel, Mater. Sci. Technol, 22 (2006) 1068-1075. https://doi.org/10.1179/174328406X114090

[15]. L. Qian, H. Toda, K. Uesugi, M. Kobayashi, T. Kobayashi, Three-dimensional visualization of ductile fracture in an Al-Si alloy by high-resolution synchrotron X-ray microtomography, Mater. Sci. Engg, (2008) 293-296. https://doi.org/10.1016/j.msea.2006.10.201

[16]. W. Ren, Z. Yang, R. Sharma, C.H. Zhang, P.J. Withers, Two-dimensional X-ray ct image based mesoscale fracture modelling of concrete, Eng. Fract. Mech, 133 (2015) 24-39. https://doi.org/10.1016/j.engfracmech.2014.10.016

[17]. T.T. Nguyen, J. Yvonnet, Q.Z. Zhu, M. Bornert, C. Chateau, A phase-field method for computational modeling of interfacial damage interacting with crack propagation in realistic microstructures obtained by microtomography, Comput. Methods Appl. Mech. Eng, 312 (2016) 567–95. https://doi.org/10.1016/j.cma.2015.10.007

[18]. B. T. Vu, A.T. Tran, D.H. Nguyen, Modeling of crack propagation in multi-phase structure by phase field method with interfacial damage, Transport and communications science Journal, 72 (2021) 911-925. https://doi.org/10.47869/tcsj.72.8.5

[19]. Q.C. He, Q. Shao, Closed-form coordinate-free decompositions of the two-dimensional strain and stress for modeling tension-compression dissymmetry, J. Appl. Mech, 86 (2019) 031007. https://doi.org/10.1115/1.4042217

[20]. G.N. Wells, L.J. Sluys, A new method for modelling cohesive cracks using finite elements, Int. J. Numer. Methods Engg, 50 (2001) 2667-2682. https://doi.org/10.1002/nme.143